

Mechanical behavior of Benxi Formation limestone under triaxial compression: a new post-peak constitutive model and experimental validation

Defeng Liu^{1,2} · Changwu Liu^{1,2} · Yaming Kang³ · Bingbing Guo^{2,4} · Yuan Jiang^{1,2}

Received: 29 September 2016 / Accepted: 31 October 2017 / Published online: 15 November 2017
© Springer-Verlag GmbH Germany, part of Springer Nature 2017

Abstract In order to understand the mechanical behavior of limestone and to formulate a new post-peak constitutive model, triaxial tests on the intact Benxi Formation limestone from Gequan mine, Hebei Province, China, were conducted using the Electro-hydraulic Servo-controlled Rock Mechanics Testing System (MTS815). Test results showed that the deformation behavior of the limestone specimens at the post-peak stage was that the axial stress dropped rapidly and the axial strain remained constant for some time before it continued to grow, but lateral strain kept increasing. To explain the deformation behavior and failure mechanism of the intact specimens, mineral composition and microstructure were analyzed using both a polarizing optical microscope and scanning electron microscopy. A tension-shear failure strength criterion was established based on the observed failure modes of the intact specimens. Furthermore, a new post-peak constitutive model was proposed according to the deformation behavior of the intact specimens at the post-peak stage. The proposed post-peak constitutive model was further developed by considering both failure strength criterion and confining pressure. In order to validate the proposed model, experimental data and theoretical results predicted by the proposed model were

compared. Comparison of results showed that the new model can capture the post-peak deformation behavior of the limestone well. Additionally, repeated loading tests under triaxial compression were performed to investigate the influence of loading times on the mechanical behavior of the fractured limestone specimens. Test results showed that both the maximum load and plastic deformation of the fractured specimens decreased with increasing loading times.

Keywords Limestone · Triaxial tests · Microstructure · Tension-shear model · Post-peak constitutive model

Introduction

Limestone is not only widely distributed in the world, it is a valuable industrial raw material (Palchik and Hatzor 2002; Atiye 2004; Gaswirth et al. 2006; Pesendorfer and Loew 2010; He et al. 2010; Rinehart et al. 2015). It is known that limestone formed by biochemical action is the main component of karst topography. This special geological condition has resulted in a large number of geological hazards associated with limestone used for human constructions (Gaswirth et al. 2006; Cardell et al. 2008; He et al. 2013; Lubelli and Nijland 2014; Cui et al. 2015; Ma et al. 2015). Two controversial issues are karst collapses and mining-induced groundwater intrusion, and both have caused severe economic loss and casualty. Therefore, the mechanical behavior of limestone has piqued researchers' interest to ensure the safety of human activities associated with limestone.

Numerous studies have been conducted to understand the mechanical behavior of the limestone. It has been found that factors such as temperature, specimen size, confining pressure, microstructure, weathering, and chemical solution highly affect the mechanical behavior of the limestone.

✉ Changwu Liu
liuchangwu@scu.edu.cn

¹ State Key Laboratory of Hydraulics and Mountain River Engineering, Sichuan University, Chengdu, Sichuan 610065, China

² College of Water Resource and Hydropower, Sichuan University, Chengdu, Sichuan 610065, China

³ School of Chemistry and Chemical Engineering, Beifang University of Nationalities, Yinchuan 750021, China

⁴ Department of Safety Engineering, Henan Institute of Engineering, Zhengzhou 450000, China

Several scholars have studied the influences of temperature on the mechanical behavior of the limestone, and they found that the yield point and strength of the limestone decreased with increasing temperature (Kılıç 2006; Nasser et al. 2013; Thongsanitgarn et al. 2014). Zhang et al. (2015) found that cracks in the limestone increased slowly below 200 °C but rapidly above 300 °C. Uniaxial compression tests on Guiting limestone with different crack lengths were conducted under different loadings (Aliha et al. 2012; Akbardoost et al. 2014). Test results showed that fracture resistance was related to the specimen size and loading conditions of the rock specimens. Triaxial tests on the limestone were also performed, and the deformation, strength, and elastic modulus increased with increasing the confining pressure (Alber and Heiland 2001; Al-Shayea 2004; He et al. 2010; Descamps et al. 2012). The transition from brittleness to ductility appeared under high confining pressure. The microstructure of the limestone was investigated using a scanning electron microscope (SEM), and the results showed that both the compressive strength and deformation behavior were controlled by the microstructure (Steve et al. 1996; Sabatakakis et al. 2008; Vajdova et al. 2010; Fornós et al. 2011; Lubelli and Nijland 2014). The weathering effect could greatly affect the pore properties of the limestone specimens, which then influences their mechanical behavior (Nicholson 2001; Atiye 2004; Cardell et al. 2008; Walbert et al. 2015). Xie et al. (2011) showed that the strength, elastic modulus, and cohesion of the limestone reduced after the specimens were saturated with the chemical solution.

Therefore, it is known from aforementioned research results that different kinds of limestone present different mechanical behaviors, even when under the same test conditions (Sabatakakis et al. 2008; Nicholson 2001; Atiye 2004). Furthermore, the mechanical behavior of the rocks is always presented through the stress-strain curves described by constitutive models (Zhou and Zhu 2010; Li et al. 2015). Unfortunately, the post-peak constitutive model of limestone has been rarely considered, even though many constitutive models have been developed for different types of rock (mudstones, sandstone, marble, shale, etc.) (Lemaitre 1984; Shah 1997; Cao et al. 2010; Cao 2012; Pourhosseini and Shabanimashcool 2014; Li et al. 2015). Zhou and Zhu (2010) proposed an elastic-plastic damage constitutive model to describe the deformation behavior of the soft rocks (mudstone, shale, etc.). Nguyen et al. (2016) deduced a constitutive model for analyzing the post-peak deformation behavior of porous sandstone on the basis of the breakage mechanics.

In this study, Benxi Formation limestone was obtained from Gequan mine, located in Hebei Province, China. To analyze the mechanical behavior of the limestone and develop a new post-peak constitutive model, triaxial tests on the intact specimens were performed using the Electro-hydraulic Servo-controlled Rock Mechanics Testing System (MTS815). The

polarizing optical microscope (POM) and SEM were used to analyze the deformation and failure behavior of the intact specimens from a microscopic view. According to macroscopic failure modes of the intact specimens, a tension-shear failure strength criterion was proposed. A new post-peak constitutive model was then established based on both the deformation behavior of the intact limestone specimens and failure strength criteria. Theoretical results were compared with the experimental results. In addition, in order to study the influence of loading times on mechanical behavior, such as the maximum load and plastic deformation, of the fractured specimens, the repeated loading tests under triaxial compression were also conducted.

Experimental studies

Description of rock specimens

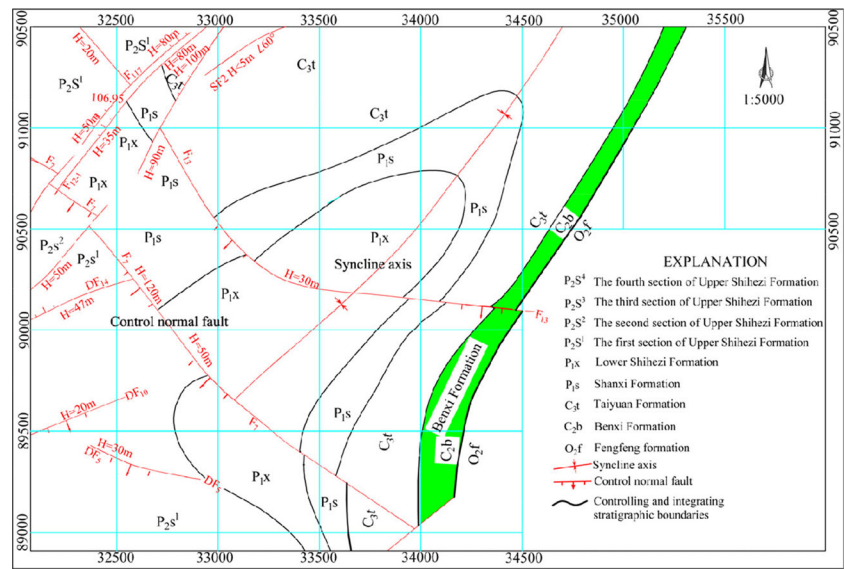
Limestone core specimens were obtained from Gequan mine, Hebei province, China. The geological framework of the mine site is shown in Fig. 1a. Limestone strata rich in confined water were located in the permo-carboniferous Benxi Formation. According to the suggestion of the International Society for Rock Mechanics and Rock Engineering (ISRM 1981) and ASTM (1986b), the rock core of the limestone was cut into cylindrical specimens measuring 50 mm in diameter and 100 mm in length. The side flatness, end flatness, and parallelism of the ends were ≤ 0.5 mm, 0.025 mm, and 0.25° , respectively. A total of 30 limestone specimens were prepared in this research, and some prepared specimens are shown in Fig. 1b.

Experimental instruments

Investigation on mineral composition of the limestone was carried out using a ZEISS Axioskop 40 microscope made in Germany. The optical diffraction approach was adopted to observe the microstructure of the specimens. This can also be used to determine the content of mineral composition by combining the Energy Dispersive Spectrometer (EDS) of the SEM. The objective lens of the equipment is used to adjust the resolution. The magnification of the microscope can be adjusted using the eyepiece.

All triaxial tests were performed using the MTS815 with a servo-controlled loading system. The maximum axial load and confining pressure are 4600 kN and 140 MPa, respectively. The data recording system can automatically collect load and the displacement data, which are recorded using an embedded axial and hoop extensometer (Fig. 2a). Axial and lateral strain can be gained by processing the obtained axial and hoop displacement data, respectively. Furthermore, two rigid steel cylinders (Fig. 2b) were placed between the loading

Fig. 1 The **a** geological framework of the mine site and **b** limestone specimens



(a) Geological framework

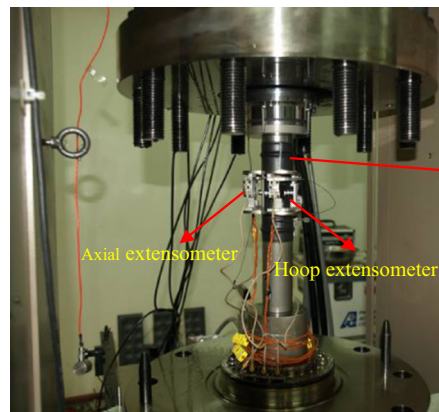


(b) Limestone specimens

frame and the specimen, which can decrease the influence of the end friction effects on the experimental results. The rock specimen and the rigid steel cylinders were jacketed by rubber tubing to separate the specimen from the confining pressure.

Investigation on the microstructure of the limestone was implemented using a Hitachi S-4800 SEM. The principle of the SEM is that the electron beam converges in the specimen surface. It can scan the entire surface of the specimen using a

Fig. 2 Experimental instruments: **a** Electro-hydraulic Servo-controlled Rock Mechanics Testing System (MTS815); **b** the force diagram of rock specimen



(a)

(b)

scanning coil. Secondary electron, back scattered electron, auger electron, and x-ray signals are generated due to the interaction between the high-power electron beam and the specimen surface. These generated electronic signals are collected and transformed into photons by the collector. The photon images are then obtained in the computer monitor using video-frequency amplifier. In addition, EDS can evaluate element types of the specimen and its content. The principle is that generated x-ray spectrums from the specimen surface arrange a different spectrum peak in the energy spectrum diagrams according to the size of energy. Element types and content are then determined according to the spectrum peak.

Experimental procedure

First, a fresh thin section of the limestone specimen was made for POM observation. Then, the thin section specimen was put on the objective stage of the microscope. Finally, the microstructure images were selected and analyzed according to the research content.

Triaxial tests (confining pressure of 5, 10, 15, and 20 MPa) on 12 intact specimens were carried out using the load and displacement control mode. Before applying the axial load control mode, the confining pressure was firstly imposed on the specimens at a constant rate of 0.4 MPa/s, which ensured that the specimen was in a uniform hydrostatic stress. Then the axial load was applied to the specimens at a constant rate of 60 kN/min before reaching peak strength (see point A in Fig. 3). After passing the peak strength, the test system adopted a displacement control mode at a constant rate of 0.15 mm/min until failure occurred.

The experimental procedure for the repeated loading tests contains two parts: forming fractured specimens and conducting triaxial tests. First, 12 intact limestone specimens were divided into three groups. According to the experimental procedure of triaxial tests on the intact specimens, triaxial tests on divided specimens were carried out at a confining pressure of 5, 10, 15, and 20 MPa. The fractured specimens were

formed when the axial stress reached the residual strength (see point B in Fig. 3) of the intact specimens. Second, displacement control mode was adopted when triaxial tests on the formed fractured specimens were performed. Each group of the fractured specimens were loaded and unloaded three times in total under the same testing condition.

First, a block body specimen of 30 mm × 30 mm × 5 mm was made for the SEM tests. Second, the specimens were plated with gold. Subsequently, the specimens were put on the specimen stage of the SEM and vacuumized. Finally, according to the research content, the specimens could be scanned and photographed at different magnifications. Microstructure images and quantitative analysis results of the element on the specimens can be obtained using SEM.

Material characterization analysis using a polarizing optical microscope (POM) and scanning electron microscope (SEM)

The specimens are gray, and the main mineral composition cannot be determined based on surface observation. In order to know the mineral composition of the limestone, microstructure investigation was performed using the POM and SEM. The microstructure images of the limestone are shown in Figs. 4 and 5.

Figure 4 shows that the specimen contains a lot of biological detritus and cement, which are called biolithite. The detritus presents either a bonded or parallel structure. The leaf-like matter in the photograph is organic matter, the structure of which is distinct and the outlines are intact. They are of different sizes and display uneven distribution. The specimen also includes a small amount of intraclasts, which are out of shape. Black mineral grains are magnetite, which are widely distributed in the specimen, and which fills the rock stylolite. Many sparry calcites exist among the biological detritus, as shown in Fig. 5. In addition, according to the testing report provided by the southwest China supervision and inspection center of mineral resources (Ministry of Land and Resources), it is known that the mineral composition in the specimen is mainly calcite (more than 95%) with some organic matter and magnetite (less than 5%).

SEM images of the specimens show that mineral composition of the intact limestone specimen is coarse-grain and microlite calcite (Fig. 5). The limestone specimen in Fig. 5a and b presents a flat and smooth surface, which indicates that the crystal structure has not been destroyed. The crystal structure of coarse-grain becomes denser as a result of a squeezing action. However, many gamma holes exist in the coarse-grain calcite of the specimen. The specimen in Fig. 5c and d shows a coarse surface with microcrystal grain, and the cement between the microcrystal consists of lots of small holes. Linkage between microlite calcite grain is loosened. Therefore, the existence of both gamma holes and

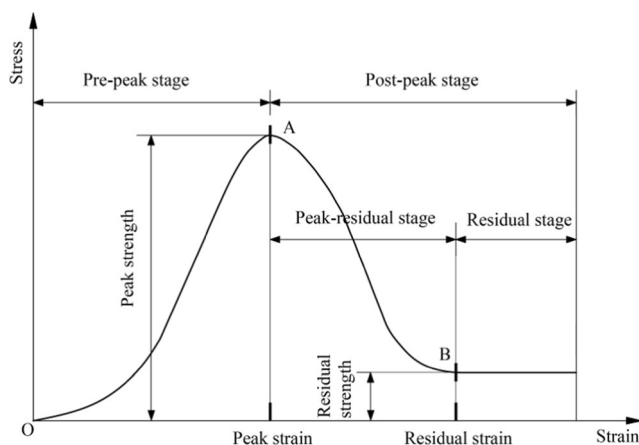
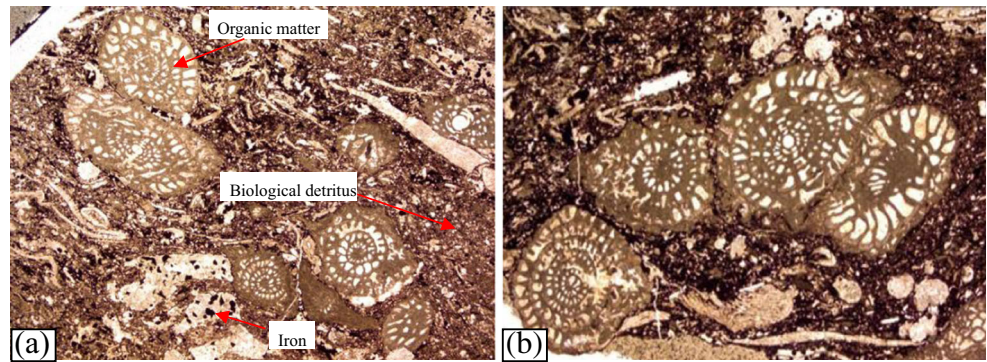


Fig. 3 Illustration of the complete stress-strain curve of the rock

Fig. 4 The microstructure of different sections on the fresh limestone (25× magnification)



microstructure features play a key role in the mechanical behavior of the limestone.

Experimental results and analysis

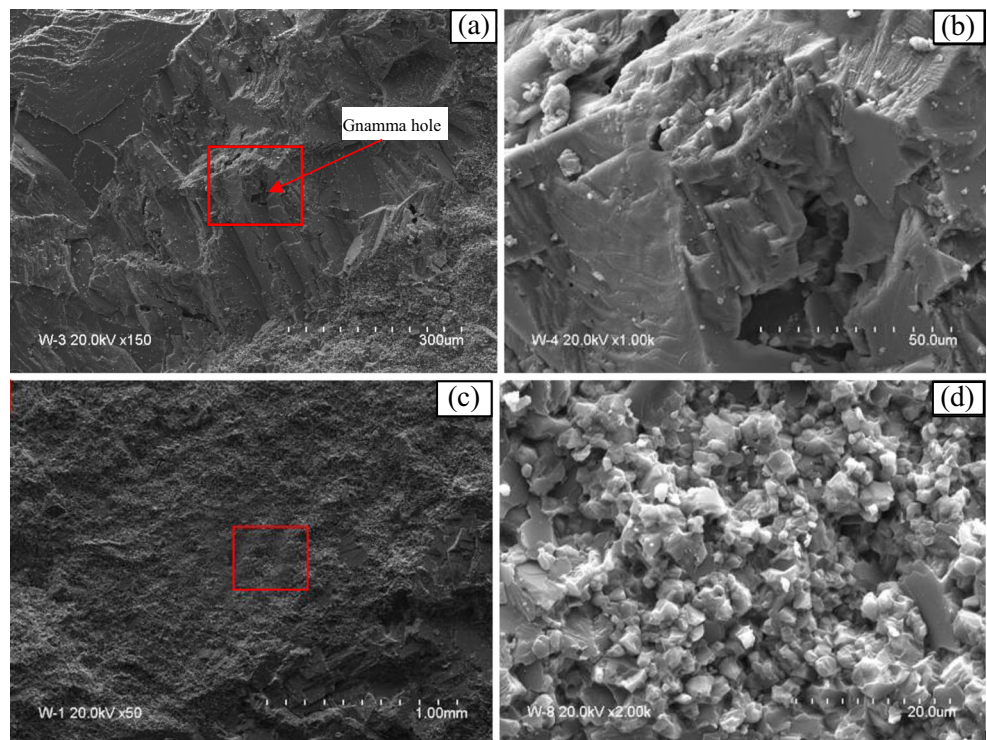
Triaxial tests on the intact limestone specimens

Figure 6a shows the complete stress-strain curves of intact limestone specimens under 5, 10, 15, and 20 MPa confining pressure. After peak strength, axial stress-strain curves showed that the axial stress dropped rapidly and the axial strain remained constant for some time before it continued to grow (see line C–D in Fig. 6b). However, axial stress-lateral strain curves showed that lateral strain kept increasing (see line E–F in Fig. 6b), and axial stress remained constant for

some time and then dropped until it returned another constant. Moreover, Fig. 6b shows that the axial strain rate is larger than the lateral strain rate prior to the point C. Thus, the peak axial strain (see point C in Fig. 6b) was larger than the peak lateral strain (see point E in Fig. 6b). In the period of the line C–D, the axial strain rate remained at zero, but the lateral strain rate increased to a certain value and remained constant. The deformation behaviors of limestone specimens were different from previous experimental results in the literature (Xie et al. 2011; Descamps et al. 2012; Parent et al. 2015), which reported that both axial and lateral strain kept increasing at the post-peak stage.

Because of the complexity of both the structure and existing environment of rock mass, some intact specimens may present abnormal behavior at the post-peak stage, such as the stress-strain relationship of the specimen under 15 MPa

Fig. 5 The microstructure of the intact limestone specimens. **a** Coarse-grain calcite with 150× magnification (scale bar is 300 μm). **b** The local amplification texture of the area of **a** marked with a red square with 1000× magnification (scale bar is 50 μm). **c** Microlite calcite with 50× magnification (scale bar is 1 mm). **d** The local amplification texture of the area of **c** marked with a red square with 2000× magnification (scale bar is 20 μm)



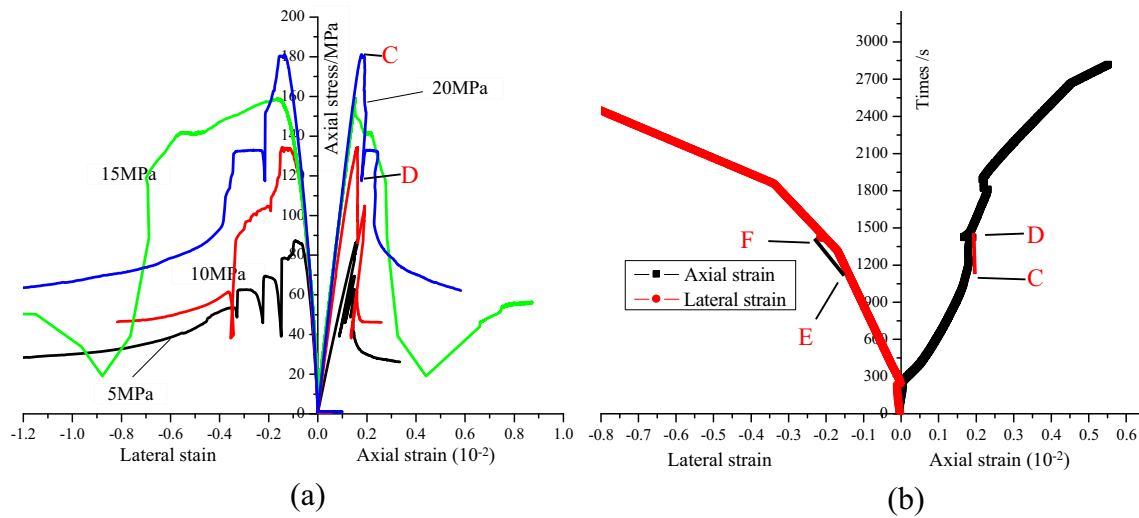


Fig. 6 Mechanical behavior of intact limestone specimens under different confining pressure. **a** Complete stress-strain curves. **b** Time-strain curve of the specimen under 20 MPa confining pressure

confining pressure (Fig. 6a). However, the elastic modulus, triaxial compressive strength, and residual strength increased with increasing confining pressure, which was consistent with the reported results (Popp and Salzer 2007; Ghazi et al. 2002; Gandomi et al. 2012). Figure 7 depicts the relationship between elastic modulus and confining pressure with a non-linear curve. The relationship between the elastic modulus and confining pressure can be obtained as follows (Eq. 1):

$$E = 21.36 + 92.73 / (1 + 10^{(0.157 \cdot (6.26 - \sigma_3))}) \quad (0 < \sigma_3 \leq 20 \text{ MPa}) \quad (1)$$

where E is the elastic modulus, and σ_3 is the confining pressure.

Figure 8 shows that peak strength and residual strength increase with increasing confining pressure. Both presented a linear relationship, and this relationship agreed with previous studies (Bhat et al. 2013; Ali et al. 2010). The relationship

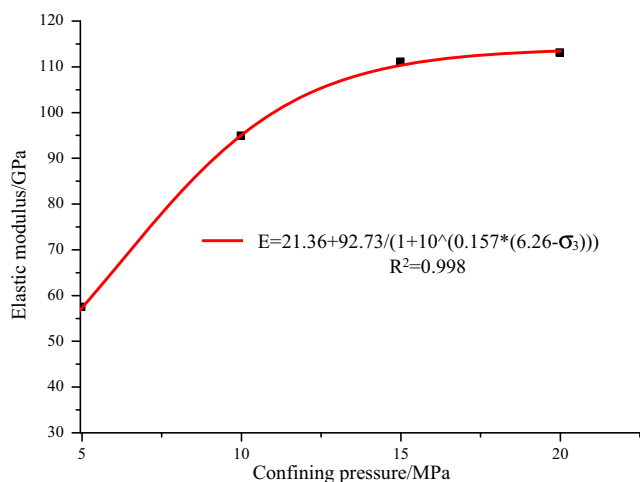


Fig. 7 Relationship between elastic modulus and confining pressure

expression between peak strength and residual strength can be characterized using Eq 2:

$$\sigma_R = e\sigma_P + f \quad (0 < \sigma_r \leq 80 \text{ MPa}) \quad (2)$$

where both e and f are constants, σ_P is the peak strength (triaxial compressive strength of the specimen), and σ_R is the residual strength (the specimen still has some bearing capacity after emerging the macro fracture). The linear fitting method is used to obtain the value of e and f . This afforded $e = 0.391$ and $f = -7.133$ with a good correlation.

Repeated loading tests on the fractured limestone specimens

Limestone strata were located in the floor of the mining coal seam in Gequan mine. Periodic weighting usually occurs

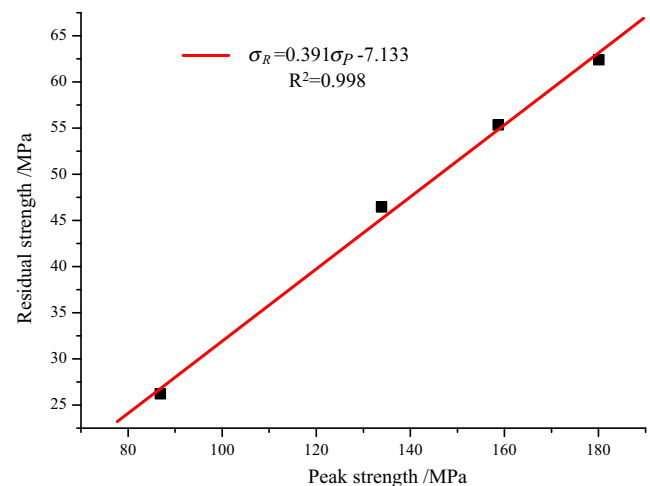


Fig. 8 Relationship between peak strength and residual strength

during retreat mining in the mine. Therefore, the top of the limestone strata may be damaged periodically because of the periodic weighting. If the maximum load of the fractured limestone strata greatly decreased with the increase in loading times (due to periodic weighting), the confined water would inrush into the working face in the mine and this would cause severe economic loss and casualty. Thus, in order to prevent confined water inrush accidents during mining, it is necessary to investigate the influence of repeated loading on the mechanical behavior of the fractured limestone specimens. Repeated loading test results on the fractured limestone specimens under different confining pressure are discussed in this section.

Figure 9 depicts that load-displacement curves of the fractured specimens show a linear trend before reaching the maximum load, which increased with increasing confining pressure. Although the displacement kept increasing, the maximum load of the fractured specimens almost kept constant, which indicated that the fractured specimens still had some bearing capacity under different confining pressures.

Figure 10 presents the influence of loading times on the maximum load of the fractured specimens under different confining pressures. It can be seen from Fig. 10 that the maximum load of the fractured specimens decreased with increased loading times. Reduced magnitude of the maximum load was larger at a low confining pressure (5 MPa). In addition, Fig. 11 shows the influence of loading times on load-displacement curves of the fractured specimens under 5 MPa of confining pressure. It was shown that the lateral displacement was larger than axial displacement. Both axial and lateral displacement decreased with increased loading times.

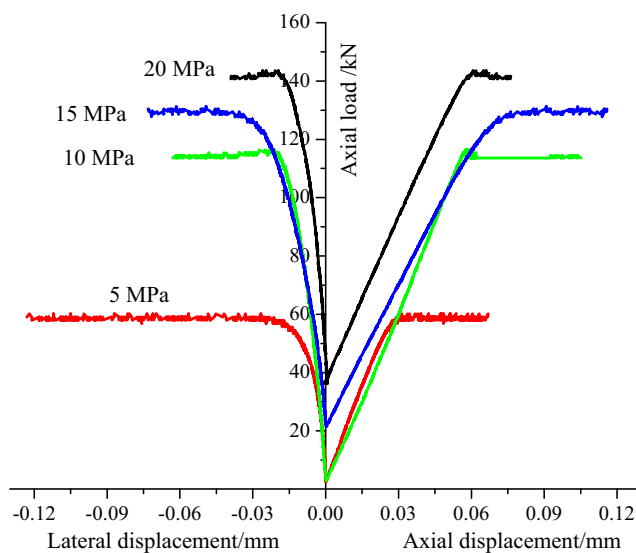


Fig. 9 Complete load-displacement curves of the fractured limestone specimens

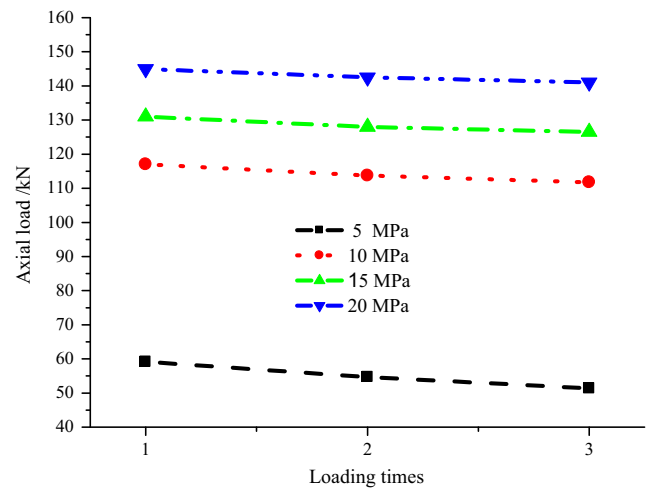


Fig. 10 Relationship between maximum load and loading times for the fractured specimens

The influence of microstructure

In order to show the influence of the microstructure on both the deformation behavior and failure mechanism of the limestone, SEM images of the fractured surface of the tested intact specimens under 10 MPa confining pressure were taken as an example for further analysis.

It can be seen from Fig. 12 that the transgranular fracture contains intracrystalline and intercrystalline fractures. Figures 12a and b show that the deformation failure of the specimen is displayed through the slip failure crossing neighboring crystals (see curves M–N and H–I in Figs. 12a and b). The curve M–N in Fig. 12a denotes that the crystals fracture presents a major direction along the axial stress direction at the pre-peak stage. The crystals around the curve H–I fractured in the lateral

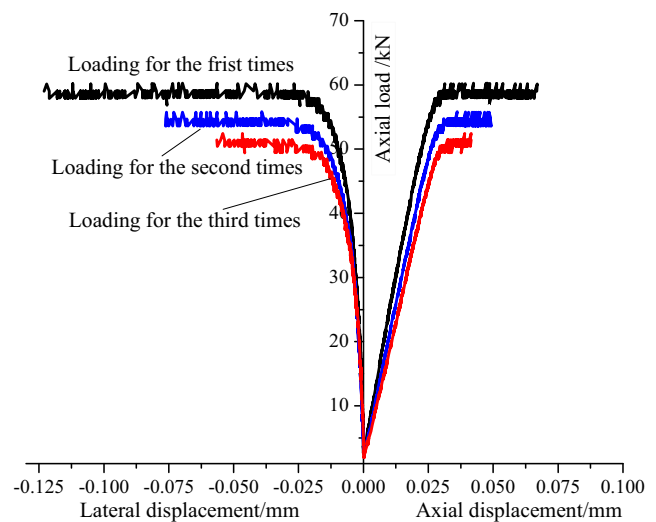
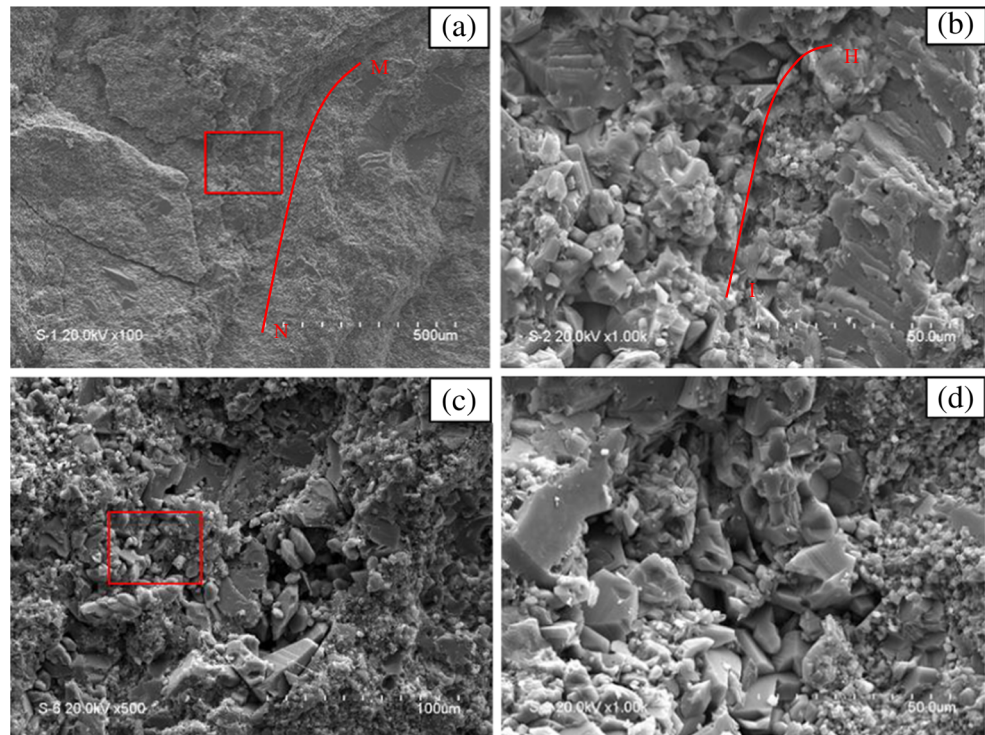


Fig. 11 Complete load-displacement curves of the fractured specimens under 5 MPa confining pressure after loading three times

Fig. 12 The microstructure of the compressed intact specimens. **a** Intracrystalline fracture texture with 100× magnification (scale bar is 500 μm). **b** The local amplification texture of the area of **a** marked with a red rectangle with 1000× magnification (scale bar is 50 μm). **c** Intercrystalline fracture texture with 500× magnification (scale bar is 100 μm). **d** The local amplification texture of the area of **c** marked with a red rectangle with 1000× magnification (scale bar is 50 μm)



direction. It is known from Fig. 5 that many gamma holes and secondary pores exist in the fresh intact limestone specimens. When the axial stress applied to the specimen kept increasing, both gamma holes and secondary pores began to evolve into new cracks (Fig. 12c). After peak strength, more and more cracks generated and propagated. The crystals along the cracks ran in the lateral direction of the limestone specimen (Fig. 12d).

Tension-shear failure strength criterion

Shear failure of the rock specimens has been extensively studied, and the Coulomb criterion was usually used to describe this failure mode (Xu 2007). However, two typical failure modes are usually observed from triaxial compression tests on the intact limestone specimens: mixed failure (tension-shear) and shear failure (Fig. 13). The mixed failure mode of the limestone specimens was observed at a low confining pressure (Figs. 13a, b, and c). The shear failure mode of the specimens was observed at a higher confining pressure (Fig. 13d). The interpretation of a tension-shear failure strength criterion on the rock specimens has not been seriously considered. In order to understand the tension-shear failure mechanism of the intact limestone specimen better, a mechanical model was proposed on the basis of the observed macro fractured surfaces of the intact specimens (Fig. 13).

Basic assumptions for the model are as follows: (1) the rupture angle on the top and bottom of the fractured surface was equal; and (2) tensile cracks went through the

axisymmetric surface of specimens. The geometry of the tension-shear failure of specimens is shown in Fig. 14.

The area of both shear failure surface (S_A) and tension failure surface (S_B) are shown in Eqs. 3 and 4, respectively.

$$S_A = \frac{\pi D^2}{4 \cos \beta} \quad (3)$$

$$S_B = D \cdot L = (2 - \tan \beta) \cdot D^2 \quad (4)$$

A local coordinate was established first, where the x-axis was parallel to the shear failure surface, and the y-axis was perpendicular to the shear failure surface. The principal stress acting on the fractured surface was decomposed along the x- and y-axis. The normal and shear stress above the shear failure surface can be obtained by Eqs. 5 and 6:

$$\sigma_y = \frac{\sigma_1 \cdot \frac{\pi D^2}{4} \cdot \cos \beta}{S_A} + \sigma_3 \sin^2 \beta + \frac{(\sigma_3 + \sigma_T) \cdot S_B \cdot \sin \beta}{S_A} \quad (5)$$

$$\tau_x = \frac{\left(\sigma_1 \cdot \frac{\pi D^2}{4} - \sigma_3 \cdot S_A \cdot \sin \beta \right) \cdot \cos \beta}{S_A} - \frac{(\sigma_3 + \sigma_T) \cdot S_B \cdot \cos \beta}{S_A} \quad (6)$$

where σ_y is the normal stress on the shear failure surface, σ_T is the tensile strength of the limestone specimens, and τ_x is the shear stress on the shear failure surface.

Replacing S_A and S_B of Eqs. 5 and 6, respectively, Eqs. 7 and 8 are obtained:

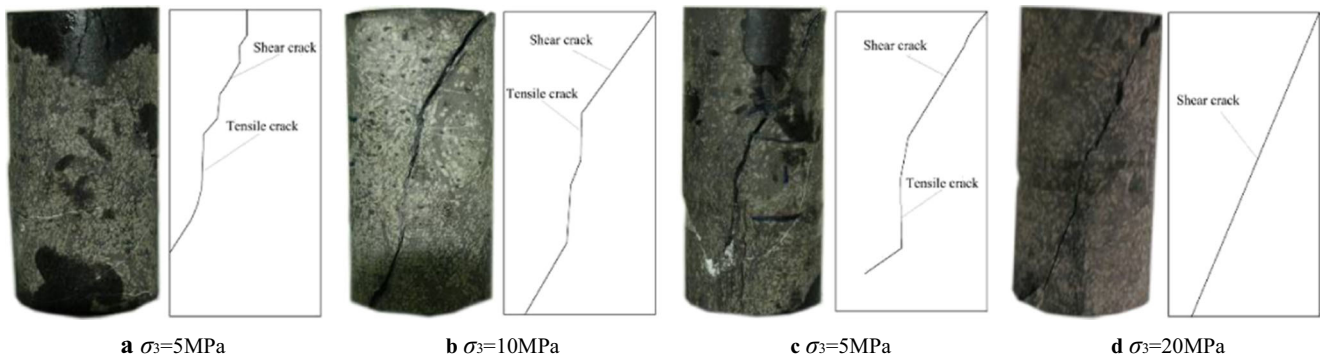


Fig. 13 Macroscopic failure modes of some compressed intact limestone specimens

$$\sigma_y = \sigma_1 \cdot \cos^2 \beta + \sigma_3 \cdot \sin^2 \beta + \frac{4(2-\tan \beta) \cdot \sin \beta \cdot \cos \beta}{\pi} (\sigma_3 + \sigma_T) \quad (7)$$

$$\tau_x = (\sigma_1 - \sigma_3) \cdot \sin \beta \cdot \cos \beta - \frac{4(2-\tan \beta) \cdot \cos^2 \beta}{\pi} (\sigma_3 + \sigma_T) \quad (8)$$

The critical value of the yield failure on the shear surface is shown in Eq. 9 (You and Hua 2001):

$$\tau_x = C + \sigma_y \cdot \tan \varphi \quad (9)$$

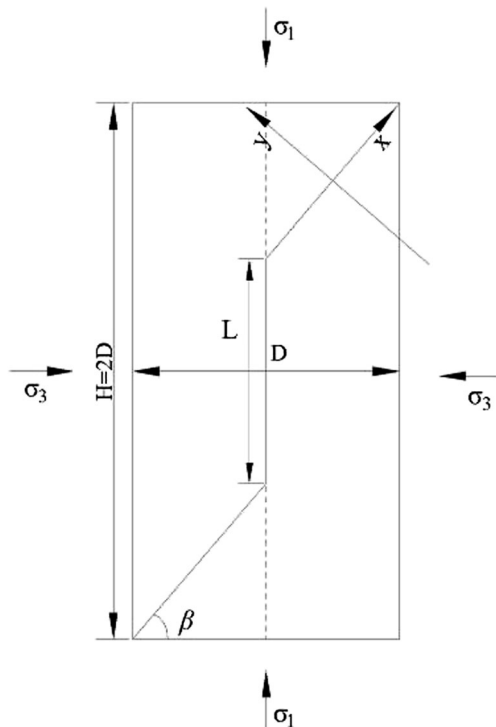


Fig. 14 The mechanical model of tension-shear failure of the rock specimens. D diameter of the specimens, L length of the tensile crack, β shear rupture angle, σ_3 confining pressure

where C is the cohesion, and φ is the internal friction angle. After substituting Eqs. 7 and 8 into Eq. 9, the expression of the peak strength can be written as Eq. 10:

$$\sigma_P = j\sigma_3 + k \cdot C + m\sigma_T \quad (10)$$

where

$$j = \frac{(\tan \varphi \tan \beta + 1) \left(\frac{4}{\pi} (2 - \tan \beta) + \tan \beta \right)}{\tan \beta - \tan \varphi};$$

$$k = \frac{1}{\cos^2 \beta (\tan \beta - \tan \varphi)};$$

$$m = \frac{4(1 + \tan \varphi \cdot \tan \beta)(2 - \tan \beta)}{\pi \cdot (\tan \beta - \tan \varphi)};$$

When L is equal to zero, shear failure dominates the specimen. In this case, Eq. 10 can be given in Eq. 11:

$$\sigma_P = k \cdot C + n\sigma_3 \quad (11)$$

where

$$k = \frac{1}{\cos^2 \beta (\tan \beta - \tan \varphi)};$$

$$n = \frac{\tan \beta + \tan \varphi \cdot \tan^2 \beta}{\tan \beta - \tan \varphi};$$

Since the rupture angle of rock specimen is $(45^\circ + \varphi / 2)$ under the shear failure mode (Qian and Shi 2003), Eq. 11 can be written as Eq. 12:

$$\sigma_P = 2C \sqrt{\frac{1 + \sin \varphi}{1 - \sin \varphi}} + \frac{1 + \sin \varphi}{1 - \sin \varphi} \sigma_3 \quad (12)$$

Equation 12 is the famous Mohr-Coulomb failure criterion expressed using the principal stress (Qian and Shi 2003), which is a special form of the tension-shear failure strength criterion (Eq. 10). The accuracy of the established tension-shear failure strength criterion is also verified well.

A new post-peak constitutive model for the limestone

Theoretical study on the constitutive model of the limestone

A constitutive model is always used to present the deformation behavior of the rocks (Lemaitre 1984; Zhou and Zhu 2010; Li et al. 2015). Cao et al. (2010) proposed a constitutive model using a statistical damage-based method to describe both the strain hardening and softening behavior of the rock. Based on the deformation behavior of the rocks, a constitutive model was established by adopting a damage statistical approach (Cao 2012). The model can describe the complete stress-strain curves of the rocks. Pourhosseini and Shabanimashcool (2014) reported a failure criterion on the basis of the dilation angle. According to the proposed failure criterion, a constitutive model was established. The model can be used to present pre-peak and post-peak deformation behavior of the intact rocks. These constitutive models are very useful for describing the pre-peak deformation behavior of the rocks. However, the post-peak deformation behavior cannot be simulated using an invariable constitutive model. In order to verify this statement, triaxial tests of the limestone specimens under 5 MPa confining pressure were taken as an example, and the predicted results from aforementioned three existing models were compared with test results, as shown in Fig. 15.

Figure 15 shows that three proposed models can describe the stress-strain relationship at the pre-peak stage well, but cannot reasonably present the deformation behavior of the limestone specimens at the post-peak stage. A reasonable post-peak constitutive model is therefore needed to describe and interpret the deformation

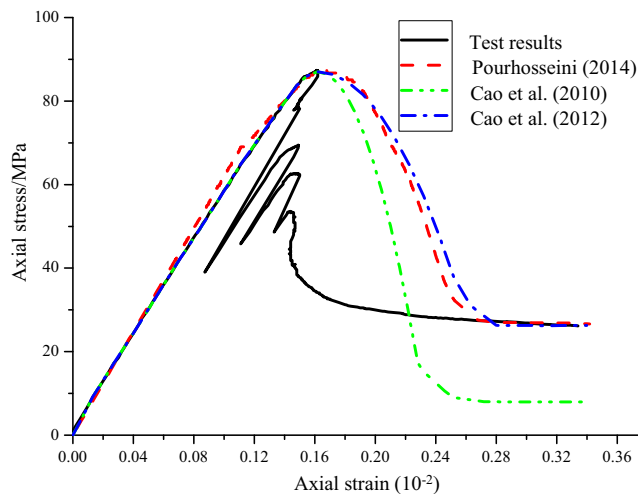


Fig. 15 Comparison between experimental and theoretical curves for the intact limestone specimen under 5 MPa confining pressure

behavior of the limestone specimens under triaxial compression.

As shown in Fig. 3, the complete stress-strain curve of the rock specimen is divided into two stages, the pre-peak and post-peak stage, and the latter can then be divided into two parts, peak-residual and residual. According to the above analysis, it is clear that the three existing constitutive models are very helpful to describe the pre-peak deformation behavior of the limestone specimens. In this study, the aforementioned statistical damage constitutive model proposed by Cao (2012) was used to simulate the stress-strain relationship of limestone specimens at the pre-peak stage. Based on the deformation behavior of the intact limestone specimens at the post-peak stage, a new post-peak constitutive model was established.

The constitutive model of the limestone specimens at the pre-peak stage can be written as Eq. 13:

$$\sigma_1 = E\varepsilon_1(1-D_1) + 2\nu\sigma_3 \quad (\varepsilon_1 < \varepsilon_{1P}) \tag{13}$$

where ε_1 is the axial strain, ε_{1P} is the axial peak strain (see Fig. 3) when axial stress is equal to the compressive strength, and ν is Poisson’s ratio. D_1 is the damage variable, which is obtained through the following expression (Eq. 14):

$$D_1 = 1 - \exp\left[-\left(\frac{F}{F_0}\right)^m\right] \tag{14}$$

where F is the micro-unit strength function, and F_0 and m are the distributed parameters of Weibull. Corresponding expressions in Eq. 14 are written as follows:

$$F = \frac{(\sigma_1 - \alpha\sigma_3) \cdot E \cdot \varepsilon_1}{\sigma_1 - 2\nu\sigma_3} - k_0;$$

$$m = 1 / \ln[E\varepsilon_{1P} / (\sigma_P - 2\nu\sigma_3)];$$

$$F_0 = F_P(m)^{1/m};$$

$$F_P = \frac{(\sigma_P - \alpha\sigma_3) \cdot E \cdot \varepsilon_{1P}}{\sigma_P - 2\nu\sigma_3} - k_0;$$

$$\alpha = \frac{1 + \sin\phi}{1 - \sin\phi};$$

$$k_0 = \frac{2C \cdot \cos\phi}{1 - \sin\phi}$$

where F_P is the micro-unit strength when axial stress is equal to the compressive strength, and C is the cohesion of the intact specimens.

It was known that the deformation behavior of limestone specimens at the post-peak stage was such that the axial stress dropped rapidly and the axial strain remained constant for some time before it continued to grow, but the lateral strain kept increasing. Moreover,

the peak axial strain was larger than the peak lateral strain. At the residual stage, the axial strain kept increasing and the residual strength of the specimens almost remained constant. Therefore, a new post-peak constitutive model can be formulated as follows (Eqs. 15b and c):

$$\begin{cases} \sigma_1 = a(\varepsilon_3 - \varepsilon_{1R})^2 + b & (\varepsilon_{1P} \leq \varepsilon_3 \leq \varepsilon_{1R}) \quad (15b) \\ \sigma_1 = \sigma_R & (\varepsilon_1 > \varepsilon_{1R}) \quad (15c) \end{cases}$$

where ε_3 is the lateral strain, and ε_{1R} is the axial residual strain (see Fig. 3) when axial stress drops to the residual strength at the post-peak stage. In addition, parameters a and b can be determined by the following conditions (Eq. 16):

$$\begin{cases} \sigma_P = a(\varepsilon_{3P} - \varepsilon_{1R})^2 + b \\ \sigma_R = a(\varepsilon_{1R} - \varepsilon_{1R})^2 + b \end{cases} \quad (16)$$

Therefore, parameters a and b were derived as follows (Eq. 17):

$$\begin{cases} a = \frac{\sigma_P - \sigma_R}{(\varepsilon_{3P} - \varepsilon_{1R})^2} \\ b = \sigma_R \end{cases} \quad (17)$$

ε_{3P} is the peak lateral strain (see Fig. 3) when axial stress is equal to the peak strength.

After substitution of Eq. 2 and Eq. 17 into Eq. 15b, the expression of Eq. 15 can be written as:

$$\begin{cases} \sigma_1 = \frac{(1-e)\sigma_P - f}{(\varepsilon_{3P} - \varepsilon_{1R})^2} (\varepsilon_3 - \varepsilon_{1R})^2 + e\sigma_P + f & (\varepsilon_{1P} \leq \varepsilon_3 \leq \varepsilon_{1R}) \quad (18b) \\ \sigma_1 = e\sigma_P + f & (\varepsilon_1 > \varepsilon_{1R}) \quad (18c) \end{cases}$$

According to above analysis, the constitutive model of the limestone is shown in Eq. 19:

$$\begin{cases} \sigma_1 = E\varepsilon_1(1-D_1) + 2\nu\sigma_3 & (\varepsilon_1 < \varepsilon_{1P}) \quad (19a) \\ \sigma_1 = \frac{(1-e)\sigma_P - f}{(\varepsilon_{3P} - \varepsilon_{1R})^2} (\varepsilon_3 - \varepsilon_{1R})^2 + e\sigma_P + f & (\varepsilon_{1P} \leq \varepsilon_3 \leq \varepsilon_{1R}) \quad (19b) \\ \sigma_1 = e\sigma_P + f & (\varepsilon_1 > \varepsilon_{1R}) \quad (19c) \end{cases}$$

Table 1 Values of the parameters in the proposed constitutive model

σ_3 (MPa)	E (GPa)	ν	C (MPa)	φ (°)	ε_{3P} (10^{-2})	ε_{1P} (10^{-2})	ε_{1R} (10^{-2})	e	f	σ_T (MPa)	β (°)	Failure mode
5	57.34						0.18				50	Tension-shear
10	95.03				0.146	0.161	0.23			5	53	Tension-shear
15	110.3	0.26	14	50			0.33	0.391	-7.133		57	Tension-shear
20	113.5						0.49				67.5	Shear

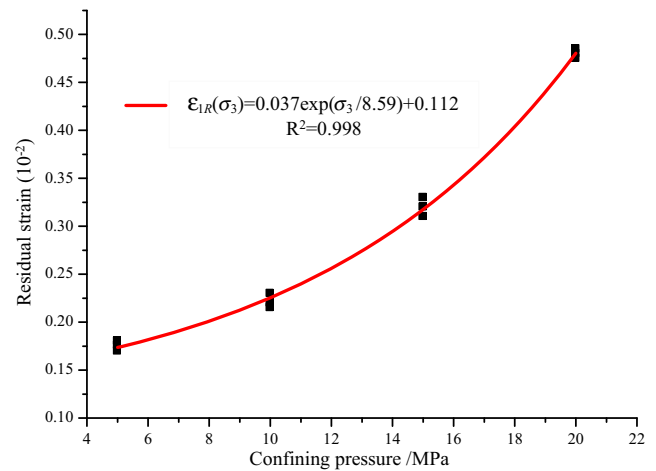


Fig. 16 Relationship between residual strain and confining pressure

Improvement of the new post-peak constitutive model

Equation 19 can only be used to describe the stress-strain relationship of the limestone specimens under a specified confining pressure. To extend the application of the new post-peak constitutive model, Eq. 19 needs to be further developed. Figure 1 shows that both the peak axial strain and lateral strain of the limestone can be treated as a constant value at a low confining pressure. Figure 16 shows that the axial residual strain of specimens increases with increasing confining pressure following an exponential relationship. The relationship between axial residual strain and confining pressure can be obtained by Eq. 20:

$$\varepsilon_{1R}(\sigma_3) = 0.037\exp(\sigma_3/8.59) + 0.112 \quad (0 < \sigma_3 \leq 20 \text{ MPa}) \quad (20)$$

Therefore, based on both Eq. 19 and two kinds of strength criteria, i.e., tension-shear and shear failure criteria, Eq. 19 can be written as:

$$\begin{cases} \sigma_1 = E\varepsilon_1(1-D_1) + 2\nu\sigma_3 & (\varepsilon_1 < \varepsilon_{1P}) \quad (21a) \\ \sigma_1 = \frac{(1-e)\sigma_P - f}{(\varepsilon_{3P} - \varepsilon_{1R}(\sigma_3))^2} (\varepsilon_3 - \varepsilon_{1R}(\sigma_3))^2 + e\sigma_P + f & (\varepsilon_{1P} \leq \varepsilon_3 \leq \varepsilon_{1R}(\sigma_3)) \quad (21b) \\ \sigma_1 = e\sigma_P + f & (\varepsilon_1 > \varepsilon_{1R}(\sigma_3)) \quad (21c) \end{cases}$$

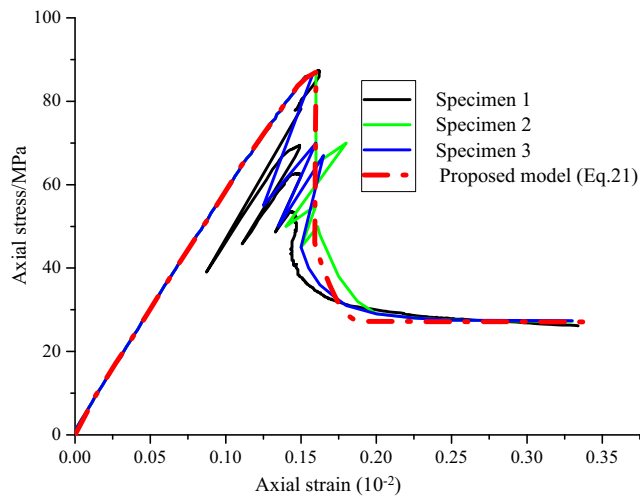


Fig. 17 Comparison between test results and theoretical results predicted by the proposed model under 5 MPa confining pressure

Where

$$\sigma_{Pi} = \begin{cases} \sigma_{P1} = j\sigma_3 + k \cdot C + m\sigma_T \\ \sigma_{P2} = 2C \sqrt{\frac{1 + \sin\varphi}{1 - \sin\varphi}} + \frac{1 + \sin\varphi}{1 - \sin\varphi} \sigma_3 \end{cases}$$

where σ_{P1} and σ_{P2} are the peak strength of the limestone specimens under the tension-shear failure and shear failure, respectively.

Validation of the proposed model

In order to validate the proposed post-peak constitutive model, all of the available test results on the intact limestone specimens under 5, 10, 15, and 20 MPa confining pressure are adopted to compare with theoretical results. The proposed model involved several parameters which can be obtained from Eq. 1, Eq. 20, and triaxial tests.

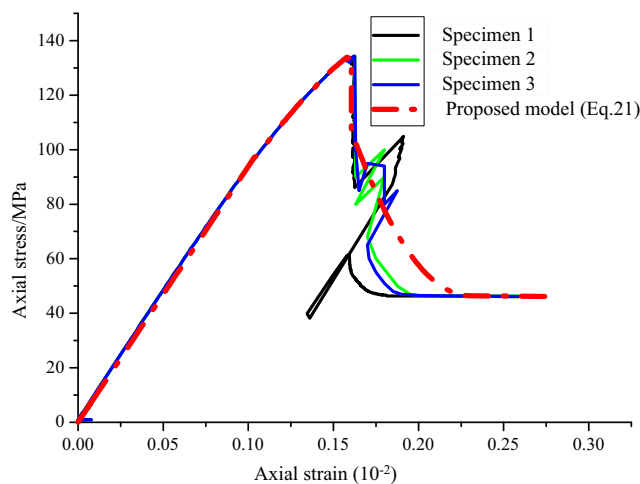


Fig. 18 Comparison between test results and theoretical results predicted by the proposed model under 10 MPa confining pressure

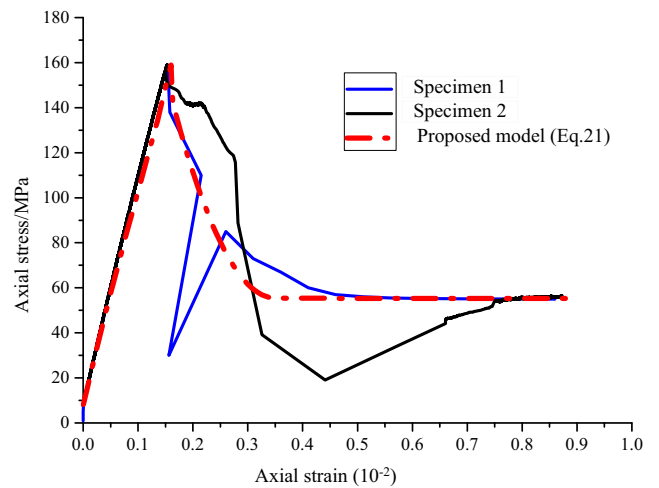


Fig. 19 Comparison between test results and theoretical results predicted by the proposed model under 15 MPa confining pressure

Elastic modulus (E) and residual strain (ε_{1R}) are obtained from Eqs. 1 and 20, respectively. The Poisson's ratio (ν) is the ratio of lateral strain to axial strain at the elastic stage of the stress-strain curve. Cohesion (C) and internal friction angle (φ) are acquired using Eq. 12 from the relationship between confining pressure and peak strength. Other parameters are derived from experimental results. The obtained parameters are shown in Table 1.

Figures 17, 18, 19, and 20 show the comparison between the test results and predicted results using the proposed model at four levels of confining pressure: 5, 10, 15, and 20 MPa. It can be seen that good agreement is obtained between the predicted results and test results. Furthermore, in contrast with common constitutive models, it is seen from Figs. 15 and 17 that the proposed post-peak constitutive model can better capture the deformation behavior of the limestone specimens at the post-peak stage.

From the discussion here, it can be seen that the proposed model has the following advantages:

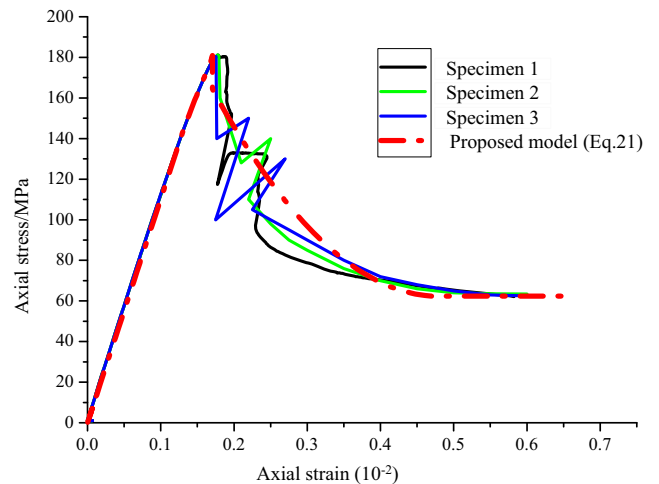
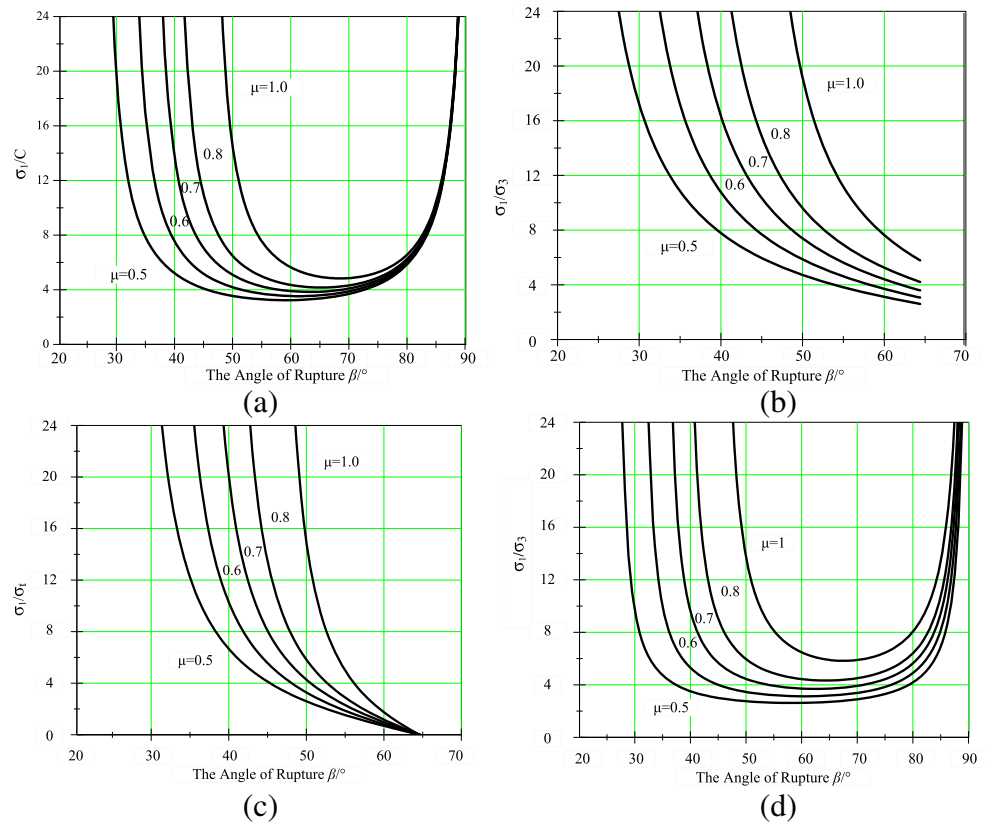


Fig. 20 Comparison between test results and theoretical results predicted by the proposed model under 20 MPa confining pressure

Fig. 21 Effects of cohesion, confining pressure, and tensile strength on the peak strength of the specimens with different rupture angle. **a** Effect of cohesion on the peak strength of the specimens under two kinds of failure modes. **b** Effect of confining pressure on the peak strength of the specimens under tension-shear failure mode. **c** Effect of tensile strength on the peak strength of the specimens under tension-shear failure mode. **d** Effect of confining pressure on the peak strength of the specimens under shear failure mode



- (1) The deformation behavior of the limestone can be properly modeled by the proposed model.
- (2) The failure modes are considered in the proposed model.
- (3) The confining pressure is considered in the proposed model.

Discussion

The tension-shear failure strength criterion was proposed according to the observation of macro fractured surfaces of the limestone specimens. Although it was valid in general, it is necessary to discuss the significance of the proposed strength criterion and study the effects of confining pressure, cohesion, and tensile strength on the peak strength of the specimens with different rupture angles.

According to Eq. 10, it is known that the peak strength is related to the internal friction angle, cohesion, confining pressure, and tensile strength. The internal friction angle is a material property, and it can be considered independently. The individual effect of cohesion, confining pressure, and tensile strength on peak strength is unrelated. So, Eq. 10 can be divided into three parts, and the corresponding relationship curves are depicted to show the influences of cohesion, confining pressure, and tensile strength on the peak strength,

respectively. Moreover, confining pressure, cohesion, and tensile strength present a linear relationship with the peak strength. Thus, their relationship can be normalized to investigate the effects of confining pressure, cohesion, and tensile strength on the peak strength of the specimen with different rupture angles. Equation 11 can also be analyzed using this method.

In order to know the differences in the peak strength of the specimens with different rupture angles between two kinds of failure strength criterion, it is necessary to make the same assumption that frictional coefficient ($\mu = \tan\varphi$) is assumed as 0.5, 0.6, 0.7, 0.8 and 1.0, respectively. Both Eq. (10) and Eq. 11 are calculated, respectively. Corresponding relationship curves are shown in Fig. 21.

It can be seen from Fig. 21a, b, and c that the peak strength of the specimens under tension-shear failure increases with an increasing frictional coefficient. However, the difference of the peak strength becomes smaller when the rupture angle (less than 64 °) increases. The cohesion, confining pressure, and tensile strength all present a linear relationship with the peak strength, which is consistent with previous studies (Popp and Salzer 2007; Gandomi et al. 2012).

As shown in Fig. 21a and d, the peak strength of the specimens under shear failure first decreases with increasing the rupture angle (25–90 °) and then increases. The frictional coefficient has little influence on the peak strength of the

specimens in a wide range of rupture angle (around $45^\circ + \varphi/2$). When $\tan \beta$ is less than μ , the peak strength increases sharply, which may result in the friction self-locking phenomenon. The peak strength of the specimens approaches infinity when the rupture angle is approximately 90° .

Comparing Fig. 21b with Fig. 21d, it can be seen that the effects of confining pressure and rupture angle on the peak strength under tension-shear failure are more notable than that under shear failure. For example, when μ is 0.5, the peak strength of the specimens with rupture angle ranging from 45° to 60° is three to six times as much as confining pressure under tension-shear failure. However, under shear failure, the peak strength is only about three times as much as confining pressure under the same condition. With the increase of the rupture angle, the difference in the peak strength of the specimens under two failure modes decreases gradually. Therefore, it is necessary to consider the failure modes of the rock when discussing the peak strength at low confining pressure.

Conclusions

Triaxial tests on the intact limestone specimens were performed to analyze the mechanical behaviors of the limestone and to develop a new post-peak constitutive model. Both POM and SEM were used to analyze the deformation behavior and failure mechanism of the intact specimens. A tension-shear failure strength criterion was established based on the observation of the macro failure modes of the intact specimens. A new post-peak constitutive model was proposed according to the post-peak deformation behavior. The proposed model was further developed by considering two kinds of strength failure criteria and confining pressure. The proposed model was also validated using experimental data. Repeated loading tests under triaxial compression were also conducted to study the influence of loading times on the mechanical behavior of the fractured limestone specimens. Several preliminary conclusions can be obtained:

- (1) The deformation behavior of the limestone specimens at the post-peak stage was that the axial stress dropped rapidly and the axial strain remained constant for some time before it continued to grow, but the lateral strain kept increasing. Moreover, the peak axial strain was larger than the peak lateral strain. Both the maximum load and plastic deformation of the fractured specimens decreased with increasing loading times.
- (2) Based on the microstructure analysis of the specimen using the POM and SEM, it was found that the limestone consists of a lot of coarse-grain and microlite calcite and contains a large number of gnamma holes and secondary pores. At the post-peak stage, the crystals along the

cracks ran in the lateral direction of the specimen, which resulted in the special deformation behavior of the limestone.

- (3) The predicted results estimated by the proposed model exhibited strong correlation with the experimental results. The new proposed post-peak constitutive model can better capture the deformation behavior of the limestone compared with common constitutive models, and it would be applicable in describing the deformation behaviors of other rocks if they presented the similar post-peak deformation behaviors with the limestone. Triaxial tests on limestone specimens were performed at low confining pressure (less than 20 MPa) to model the actual situation in the Gequan mine. If the project were to be carried out under higher in situ stress conditions in the future, more triaxial tests would be needed to adjust Eqs. 1 and 20 and to further verify the validity of the proposed model.

Acknowledgments The authors would like to acknowledge the financial support of the National Basic Research Program of China (973 Program) (Grant No: 2010CB226802) and National Natural Science Foundation-Coal Joint Fund of China (Grant No: 51134018).

References

- Akbardoost J, Ayatollahi MR, Aliha MRM, Pavier MJ, Smith DJ (2014) Size-dependent fracture behavior of Guiting limestone under mixed mode loading. *Int J Rock Mech Min Sci* 71:369–380
- Alber M, Heiland J (2001) Investigation of a limestone pillar failure part 1: geology, laboratory testing and numerical modeling. *Rock Mech Rock Eng* 34(3):167–186
- Ali MSM, Oehlers DJ, Griffith MC (2010) The residual strength of confined concrete. *Adv Struct Eng* 13(4):603–618
- Aliha MRM, Sistaniniab M, Smith DJ, Pavier MJ, Ayatollahi MR (2012) Geometry effects and statistical analysis of mode I fracture in guiting limestone. *Int J Rock Mech Min Sci* 51:128–135
- Al-Shayea NA (2004) Effects of testing methods and conditions on the elastic properties of limestone rock. *Eng Geol* 74(1–2):139–156
- ASTM (1986) Standard test method for triaxial compressive strength of undrained rock core specimens without pore pressure measurement. ASTM Standard 04.08 (D2664). ASTM International, West Conshohocken
- Atiye T (2004) The effect of weathering on pore geometry and compressive strength of selected rock types from Turkey. *Eng Geol* 75:215–227
- Bhat DR, Bhandary NP, Yatabe R (2013) Experimental study of strength recovery from residual strength on kaolin clay. *Int J Civ Eng* 7(1): 67–73
- Cao WG, Zhao H, Li X et al (2010) Statistical damage model with strain softening and hardening for rocks under the influence of voids and volume changes. *Can Geotech J* 47(8):857–871
- Cao W (2012) A statistical damage simulation method for rock full deformation process with consideration of the deformation characteristics of residual strength phase. *China Civ. Eng J* 45(6):139–145
- Cardell C, Benavente D, Rodríguez-Gordillo J (2008) Weathering of limestone building material by mixed sulfate solutions. Characterization of stone microstructure, reaction products and decay forms. *Mater Charact* 59(10):1371–1385

- Cui QL, Wu HN, Shen SL, Xu YS, Ye GL (2015) Chinese karst geology and measures to prevent geohazards during shield tunnelling in karst region with caves. *Nat Hazards* 77(1):129–152
- Descamps F, Silva MRD, Schroeder C et al (2012) Limiting envelopes of a dry porous limestone under true triaxial stress states. *Int J Rock Mech Min Sci* 2012(56):88–99
- Fornós JJ, Gómez-Pujol L, Cifre J et al (2011) First steps in limestone weathering and erosion: an atomic force microscopy (AFM) and scanning electron microscopy (SEM) approach. *Acta Carsologica* 40:275–282
- Gandomi AH, Babanajad SK, Alavi AH, Farnam Y (2012) Novel Approach to Strength Modeling of Concrete under Triaxial Compression. *J Mater Civil Eng* 24(9):1132–1143
- Gaswirth SB, Budd DA, Crawford BR (2006) Textural and stratigraphic controls on fractured dolomite in a carbonate aquifer system, Ocala limestone, west-central Florida. *Sediment Geol* 184:241–254
- Ghazi M, Attard MM, Foster SJ (2002) Modelling triaxial compression using the Microplane formulation for low confinement. *Comput Struct* 80(11):919–934
- He KQ, Jia YY, Wang B, Wang RL, Luo HL (2013) Comprehensive fuzzy evaluation model and evaluation of the karst collapse susceptibility in Zaozhuang region, China. *Nat Hazards* 68(2):613–629
- He MC, Miao JL, Feng JL (2010) Rock burst process of limestone and its acoustic emission characteristics under true-triaxial unloading conditions. *Int J Rock Mech Min Sci* 47(2):286–298
- ISRM (1981) ISRM suggested methods for rock characterization, testing and monitoring. Pergamon, Oxford, pp. 113–116 and 123–127
- Kılıç Ö (2006) The influence of high temperatures on limestone P-wave velocity and Schmidt hammer strength. *Int J Rock Mech Min Sci* 43(6):980–986
- Lemaitre J (1984) How to use damage mechanics. *Nucl Eng Des* 80(2):233–245
- Li Y, Oh J, Mitra R et al (2015) A constitutive model for a laboratory rock joint with multi-scale asperity degradation. *Comput Geotech* 72:143–151
- Lubelli B, Nijland TG (2014) Damage mechanism in Tournai limestone—the case of the tomb of admiral tromp in the old Church of Delft (the Netherlands). *J Cult Herit* 15:313–317
- Ma D, Bai HB, Wang YM (2015) Mechanical behavior of a coal seam penetrated by a karst collapse pillar: mining-induced groundwater inrush risk. *Nat Hazards* 75(3):2137–2151
- Nasser MHB, Goodfellow SD, Wanne T et al (2013) Thermo-hydro-mechanical properties of Cobourg limestone. *Int J Rock Mech Min Sci* 61(10):212–222
- Nguyen GD, Chi TN, Bui HH et al (2016) Constitutive modelling of compaction localisation in porous sandstones. *Int J Rock Mech Min Sci* 83:57–72
- Nicholson DT (2001) Pore properties as indicators of breakdown mechanisms in experimentally weathered limestones. *Earth Surf Proc Land* 26:819–838
- Palchik V, Hatzor YH (2002) Crack damage stress as a composite function of porosity and elastic matrix stiffness in dolomites and limestones. *Eng Geol* 63:233–245
- Parent T, Domede N, Sellier A, Mouatt L (2015) Mechanical characterization of limestone from sound velocity measurement. *Int J Rock Mech Mining Sci* 79:149–156
- Pesendorfer M, Loew S (2010) Subsurface exploration and transient pressure testing from a deep tunnel in fractured and karstified limestones (Lötschberg Base tunnel, Switzerland). *Int J Rock Mech Min Sci* 47(1):121–137
- Popp T, Salzer K, (2007) Anisotropy of seismic and mechanical properties of Opalinus clay during triaxial deformation in a multi-anvil apparatus. *Phys Chem Earth Parts A/B/C* 32(8–14):879–888
- Pourhosseini O, Shabanimashcool M (2014) Development of an elasto-plastic constitutive model for intact rocks. *Int J Rock Mech Min Sci* 66:1–12
- Qian MG, Shi PW (2003) Mining pressure and strata control. China Mining University Press, Xuzhou, pp 23–26
- Rinehart AJ, Bishop JE, Thomas D (2015) Fracture propagation in Indiana limestone interpreted via linear softening cohesive fracture model. *J Geophys Res* 120(4):2292–2308
- Sabatokakis N, Koukis G, Tsiambaos G et al (2008) Index properties and strength variation controlled by microstructure for sedimentary rocks. *Eng Geol* 97:80–90
- Shah KR (1997) An elasto-plastic constitutive model for brittle-ductile transition in porous rocks. *Int J Rock Mech Min Sci* 34(3–4):283.e1–283.e13
- Steve DL, Reddy MM, Fred Ramirez W et al (1996) Limestone characterization to model damage from acidic precipitation: effect of pore structure on mass transfer. *Environ Sci Technol* 30(7):2202–2210
- Thongsanitgarn P, Wongkeo W, Chaipanich A et al (2014) Heat of hydration of Portland high-calcium fly ash cement incorporating limestone powder: effect of limestone particle size. *Constr Build Mater* 66(36):410–417
- Vajdova V, Zhu W, Chen TMN et al (2010) Micromechanics of brittle faulting and cataclastic flow in Tavel limestone. *J Struct Geol* 32:1158–1169
- Walbert C, Eslami J, Beaucour A, Bourges A (2015) Evolution of the mechanical behaviour of limestone subjected to freeze–thaw cycles. *Environ Earth Sci* 74(7):6339–6351
- Xie SY, Shao JF, Xu WY (2011) Influences of chemical degradation on mechanical behaviour of a limestone. *Int J Rock Mech Min Sci* 48(5):741–747
- Xu ZY (2007) Rock mechanics. China Water Power Press, Beijing, pp 47–50
- You MQ, Hua AZ (2001) Strength criterion and internal frictional coefficient of rock specimen (in Chinese). *J Geom* 7(1):53–60
- Zhang W, Qian H, Sun Q et al (2015) Experimental study of the effect of high temperature on primary wave velocity and microstructure of limestone. *Environ Earth Sci* 74(7):5739–5748
- Zhou CY, Zhu FX (2010) An elasto-plastic damage constitutive model with double yield surfaces for saturated soft rock. *Int J Rock Mech Min Sci* 47(3):385–395